Electrical conduction processes in aluminum: Defects and phonons

Kashi N. Subedi,[1,*] Keerti Kappagantula,[2] Frank Kraft,[3] Aditya Nittala,[2] and David A. Drabold[1,†]
[1]*Department of Physics and Astronomy, Nanoscale and Quantum Phenomena Institute, Ohio University, Athens, Ohio 45701, USA*
[2]*Pacific Northwest National Laboratory, Richland, Washington 99352, USA*
[3]*MetalKraft Technologies, Albany, Ohio 45710, USA*

(Received 9 February 2022; revised 14 March 2022; accepted 17 March 2022; published 31 March 2022)

It is well known that disorder (structural or thermal) induces electronic scattering processes which determine the resistivity of crystalline metals. In this paper, we employ a variant of the Kubo-Greenwood formula to compute the space-projected conductivity and study the atomistic details of conduction in models of crystalline aluminum within the framework of density functional theory. We consider point and extended lattice defects and show with spatial detail *how* the defect locally affects conduction. We simulate thermal disorder and determine how the disorder affects the conductivity in real space and reveal the spatial nature of thermal fluctuations. Furthermore, we show that well below the Debye temperature, a classical thermal molecular dynamics simulation reproduces the form of temperature-dependent conductivity predicted by the Bloch-Grüneisen formula.

DOI: 10.1103/PhysRevB.105.104114

I. INTRODUCTION

Transport theory in metals is one of the classic stories of science. The Boltzmann transport equation [1,2] estimates the dynamics of the electronic distribution function, taking into account external fields and the collision processes. With the development of quantum mechanics, Sommerfeld introduced Fermi-Dirac statistics and a free-electron model [3]. Houston [4] and Frenkel and Mirolubow [5] discussed scattering of electron waves by crystals, but it was Bloch who established the basis of the modern theory of metallic electrons [6]. Quantum mechanical theories of transport in liquid metals appeared in the 1950s [7] and were a substantial development over earlier models.

From a different point of view—the statistical mechanics of linear response—Kubo explored the linear response of a material to an external AC electric field [8]. The resulting expression for the electrical conductivity, further approximated within a single-particle picture of the electronic structure, is known as the Kubo-Greenwood formula (KGF). This was later generalized as the "fluctuation-dissipation theorem" that mathematically connects the dissipative process with fluctuations for systems near equilibrium [9]. The KGF has become a widely used method to compute electronic conductivity. It has been implemented in the Green's function formalism [10,11] and density functional theory (DFT) [12–19] with great success. An *ab initio* estimate of the temperature dependence of conductivity on amorphous solids has also been obtained from KGF [15]. Where metals are concerned, the KGF has been employed to compute the conductivity of highly disordered or liquid metals [17,18]. To our knowledge, no attempt has been made to compute the temperature dependence of the conductivity in a low-temperature range that represents a weakly disordered phase of the metal. It is known from experiments that the resistivity of simple metals closely follow the Bloch-Grüneisen T^5 law at low temperatures [20], analogous to Debye's form for the specific heat.

DFT methods have been used to study lattice defects in metals. There have been studies ranging from the structural stability of defects [21] to charge transport [22]. However, a full atomistic grasp of conduction with defects in metals is lacking. It is of interest to know quantitatively *how* the conduction is spatially affected by such defects. Recently, we devised a method to exploit the KGF in a different way to determine the conduction-active elements of materials exploiting a spatial decomposition of the KGF. We dubbed this the "space-projected conductivity" (SPC). We have applied the method to several problems in mixed semiconducting systems (for example, conducting bridge computer memory materials [23–26]). These computations identify conduction pathways in heterogeneous materials and provide useful information for problems of material design. We also reported conduction fluctuations in liquid silicon [27]. Here, we extend this type of analysis to fcc aluminum, with defects and thermal disorder. In one of our earlier works, we observed a uniform spatial distribution of conduction in crystalline Al [27]. We also showed that the spectrum of conduction eigenvalues for this metal possesses an extended tail that is absent in semiconductor/insulating systems.

In this paper, we study two different processes that affect the conductivity of metals. First, we discuss thermal disorder using a quantum molecular dynamics approach at a chosen temperature and use the KGF method to compute the conductivity. We show that the KGF correctly predicts the form of the temperature dependence of the conductivity. Second, we discuss the role of lattice defects in the conduction of the metal. We show that reduction of conduction due to defects is substantial and produce estimates for the spatial range of

*ks173214@ohio.edu
†drabold@ohio.edu

"conduction damage" induced by these defects. For this, we consider two different types of defects, namely, vacancies and the grain boundaries (GBs). For vacancies, we keep our analysis simple by considering a single vacancy and a divacancy in a single crystal. For GBs, we consider two symmetric tilt grain boundary models and visualize conduction pathways in the vicinity of these GBs. To study the conduction near the vacancies and GBs, we utilize our recently proposed method to project conductivity onto real space [23].

The rest of this paper is organized as follows. In Sec. II, we discuss the details of the models and computational methodologies employed in this paper. In Sec. III, we provide the results for the electronic conduction processes for different kinds of defects present in aluminum. We summarize our findings in Sec. IV.

II. MODELS AND METHODS

A. Simulation of thermal disorder

To estimate the effects of thermal disorder on conduction, we created a $4 \times 4 \times 4$ structure from the fcc primitive cell to form a supercell with 256 atoms. To model thermal disorder, we simply average the KGF over a constant-temperature MD simulation. For any MD snapshot, the thermal disorder induces inhomogeneous conduction in space, as gauged by the SPC. Such a procedure is obviously suspect for $T < \Theta_D$, with Θ_D being the Debye temperature, and must fail as $T \to 0$ as the classical dynamics freeze-out. How this crude approximation is reasonable to a temperature lower than Θ_D in the sense that the resistivity given by experiment or the Bloch-Grüneisen formula is well reproduced is of interest.

We implemented *ab initio* molecular dynamics simulations (AIMD) to obtain representative models at different temperatures. Snapshots of the Al crystal at a selected temperature T were obtained by equilibrating the cell and sampling steps near the end of a 2 ps run. A time step of 1.5 fs was used, and the temperature was controlled by a Nosé-Hoover thermostat [28–30]. The last configuration from each temperature was used as a starting configuration for the succeeding temperature. For each temperature, the last 10 configurations at an interval of 10 steps (15 fs) were chosen for the conductivity calculations. Static calculations were performed at four **k** points sampled on the first Brillouin zone using the Monkhorst-Pack scheme.

B. Defects

1. Vacancies

For this case, we constructed a $5 \times 5 \times 5$ structure from the fcc primitive cell, yielding a cubic supercell 20.25 Å on a side and consisting of 500 atoms. Single vacancies and divacancies were then created by removing an atom(s) from the supercell. For these larger models with vacancies, static calculations were performed at the Γ point.

2. Grain boundaries

We also considered a few possible GBs. GBs are often described by the nomenclature Σ, tilt/twist angles, symmetric/asymmetric GBs, crystallographic directions, and specification of GB planes. The term Σ corresponds to the reciprocal of the density of the coincident site lattice (CSL). For example, Σ5 has 1/5 of the atoms in the CSL. The tilt boundaries are often described by a shared tilt axis that lies within the grain boundary plane, e.g., ⟨1 0 0⟩, and either one (symmetric) or two (asymmetric) planes. For further information on the crystallography of the GBs and the CSL, the reader is referred to Refs. [31,32]. We created two symmetric grain boundary models, namely, Σ5 {0 −3 1} ⟨1 0 0⟩ and Σ13 {0 −2 3} ⟨1 0 0⟩. The misorientation angles for these grain boundary models are 36.87° and 22.62°, respectively. In these models, there are two GBs, one at the middle of the supercell and the other at the interface of the boundaries parallel to the middle GB because of the periodic boundary conditions. The distance between the middle and interface GBs was kept at a distance of at least 25 Å to minimize the interactions between these GBs. This resulted in orthorhombic supercells with 936 and 816 atoms, respectively. Fifty initial structures for each GB were obtained by translating atoms slightly along the GB plane. The minimum distance between the Al atoms at the GB was no less than 2.56 Å. For these 50 structures, zero-pressure relaxations were done separately using the conjugate gradient method, and the structure with minimum energy was chosen. Since the cells were large, relaxations were performed with LAMMPS using the embedded-atom method potential [33]. The force acting on each atom was computed using the Vienna Ab initio Simulation Package (VASP) for these relaxed models and was relatively small (0.01 eV/Å). Static calculations were then performed using VASP to obtain the information for conductivity calculations.

C. Energy functionals and electron-ion interactions

The AIMD calculations were performed using VASP [34]. A plane-wave basis set was used with a kinetic energy cutoff of 250 eV. For static calculations, a larger cutoff of 320 eV was used. We used projected augmented wave potentials [35] to account for the ion-electron interaction and the generalized gradient approximation of Perdew, Burke, and Ernzerhof [36] as the exchange-correlation functional.

D. Space-projected conductivity

In this section, we summarize a method to project electronic conductivity onto real-space grids by exploiting the KGF [8,37]. The average conductivity from the diagonal elements of the conductivity tensor for any frequency ω can be expressed as

$$\sigma(\omega) = \frac{2\pi e^2}{3m^2\Omega\omega} \sum_{\mathbf{k}} w_{\mathbf{k}} \sum_{i,j} \sum_{\alpha} [f(\epsilon_{i,\mathbf{k}}) - f(\epsilon_{j,\mathbf{k}})] \times |\langle \psi_{j,\mathbf{k}} | p^{\alpha} | \psi_{i,\mathbf{k}} \rangle|^2 \delta(\epsilon_{j,\mathbf{k}} - \epsilon_{i,\mathbf{k}} - \hbar\omega). \quad (1)$$

In Eq. (1), e and m represent the charge and mass of the electron, respectively. Ω is the volume of the supercell, and ω is the frequency. Here, $w_{\mathbf{k}}$ are the **k**-point integration weights. $\psi_{i,\mathbf{k}}$ is the non-spin-polarized Kohn-Sham orbital associated with energy $\epsilon_{i,\mathbf{k}}$, and $f(\epsilon_{i,\mathbf{k}})$ denotes the Fermi-Dirac weight. p^{α} is the momentum operator along each Cartesian direction α. Let us rewrite Eq. (1) with terms involving energies (bands)

and the spatial part α separately,

$$\sigma = \sum_{\mathbf{k}} w_{\mathbf{k}} \sum_{i,j,\alpha} g_{ij,\mathbf{k}} \, |\langle \psi_{j,\mathbf{k}} | p^{\alpha} | \psi_{i,\mathbf{k}} \rangle|^2, \tag{2}$$

where

$$g_{ij,\mathbf{k}} = \frac{2\pi e^2}{3m^2\Omega\omega}[f(\epsilon_{i,\mathbf{k}}) - f(\epsilon_{j,\mathbf{k}})]\delta(\epsilon_{j,\mathbf{k}} - \epsilon_{i,\mathbf{k}} - \hbar\omega).$$

To project the conductivity onto real space, Eq. (2) is written in the position representation with x and x' as dummy variables:

$$\sigma = \sum_{\mathbf{k},i,j,\alpha} w_{\mathbf{k}} \, g_{ij,\mathbf{k}} \int d^3x \int d^3x' [\psi^*_{j,\mathbf{k}}(x) p^{\alpha} \psi_{i,\mathbf{k}}(x)] \times [\psi^*_{j,\mathbf{k}}(x') p^{\alpha} \psi_{i,\mathbf{k}}(x')]^*. \tag{3}$$

If we define complex-valued functions $\xi^{\alpha}_{ji,\mathbf{k}}(x) = \psi^*_{j,\mathbf{k}}(x) p^{\alpha} \psi_{i,\mathbf{k}}(x)$ on a real-space grid (call the grid points x) with uniform spacing of width h in three dimensions, then we can approximate the integrals as a sum on the grids. Thus, Eq. (3) can be written as

$$\sigma \approx h^6 \sum_{x,x'} \sum_{\mathbf{k},i,j,\alpha} w_{\mathbf{k}} \, g_{ij,\mathbf{k}} \, \xi^{\alpha}_{ji,\mathbf{k}}(x) \left[\xi^{\alpha}_{ji,\mathbf{k}}(x')\right]^*. \tag{4}$$

In the preceding equation, the approximation becomes exact as $h \to 0$. If we define a Hermitian, positive-semidefinite matrix

$$\Gamma(x,x') = h^6 \sum_{\mathbf{k},i,j,\alpha} w_{\mathbf{k}} \, g_{ij,\mathbf{k}} \, \xi^{\alpha}_{ji,\mathbf{k}}(x) \left[\xi^{\alpha}_{ji,\mathbf{k}}(x')\right]^*, \tag{5}$$

we can spatially decompose the conductivity at each grid point as $\zeta(x) = |\sum_{x'} \Gamma(x,x')|$. $\zeta(x)$ contains vital information about the conduction-active parts of the system. We showed elsewhere that the eigenvectors of Γ provide a convenient and often compact description of electronic conduction [27].

To implement the method, we used VASP and associated Kohn-Sham orbitals $\psi_{i,\mathbf{k}}$; nevertheless, the method is suitable for any appropriate basis sets. A grid spacing in the range of ≈0.3–0.5 Å was used. We then projected the wave function corresponding to each band onto a grid point [38]. ξ^{α}_{ji} are obtained using a centered finite-difference method to compute the gradient of ψ_i with respect to the α direction. We have averaged over Cartesian indices α. We used an electronic temperature of $T = 1000$ K in the Fermi-Dirac distribution. The δ function in Eq. (1) is approximated by Gaussian distributions of different widths in the range 0.005–0.04 eV, which we discuss in more detail below. The impact on the conductivity due to different factors such as the smearing width, number of atoms, smearing temperature, and energy cutoff for finite-size cells is discussed in Refs. [18,19,39].

III. RESULTS AND DISCUSSION

A. Temperature dependence of the conductivity

In this section, we study the effects of thermal disorder on conductivity. We first present the results of thermally averaging the KGF to estimate the T dependence of the conductivity and then briefly discuss the spatial distribution of conduction

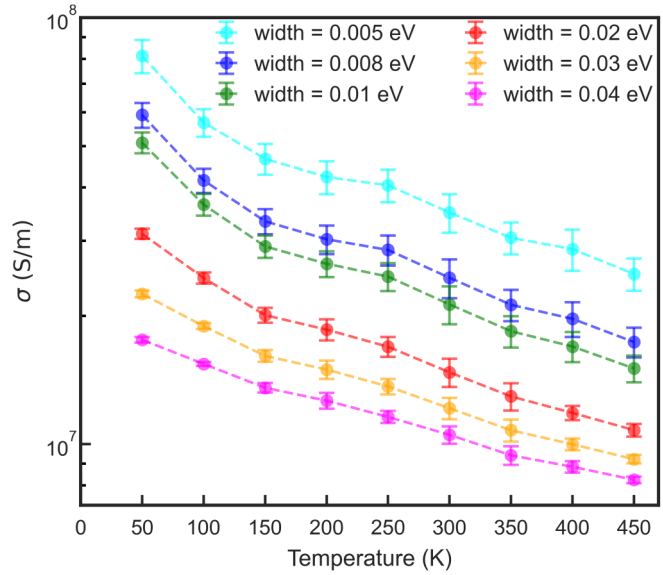

FIG. 1. Electronic conductivity (logarithmic scale) computed using the Kubo-Greenwood formula at different temperatures. The bars correspond to standard deviation from the mean conductivity averaged from the last 10 snapshots that are 15 fs apart at the end of 2 ps MD. "Width" in the legend refers to the values of smearing widths used in the Gaussian distribution function to approximate the δ function in Eq. (1).

at two different temperatures: one at room temperature and the other near the melting point.

Figure 1 shows the thermally averaged conductivity computed using the KGF from the last 10 snapshots of 2 ps annealing. From Fig. 1, we see that the value of the conductivity is sensitive to the choice of smearing width; nevertheless, the shape of the conductivity as a function of T is not much affected (although the value of the conductivity varies by a factor of ≈4 over the range of widths selected). In our previous work, we observed conductivities within a factor of 10 (or better). This is not surprising in view of the sensitivity of the conductivity to cell size effects, **k** points, intrinsic limitations of the KGF, etc. [15,40]. One of the well-known challenges of KGF calculations is handling the δ function in Eq. (1). For a supercell, the number of states near the Fermi level E_F scales with the number of atoms. For small cells and defective semiconductors, for example, there will be inadequate sampling of the relevant states, so that some strategy is required to mimic the thermodynamic limit. The most obvious expedient is to simply broaden the δ function to include more states near E_F. On the other hand, for metals like Al, there is a large number of bands near E_F even for our small supercells. For the chosen models in our calculations, we observe that the splitting of these states lies within ≈0.01–0.03 eV and is affected by the temperature. Conductivities with smearing widths of 0.01 eV and smaller are mostly attributed to intraband transitions and are closely analogous to Drude conductivity. Since the conductivity follows almost the same trend for the selected smearing widths, we fitted the resistivity derived from the KGF with the Bloch-Grüneisen formula [41] for a smearing width of 0.02 eV, which includes the contributions from both intra- and interband transitions.

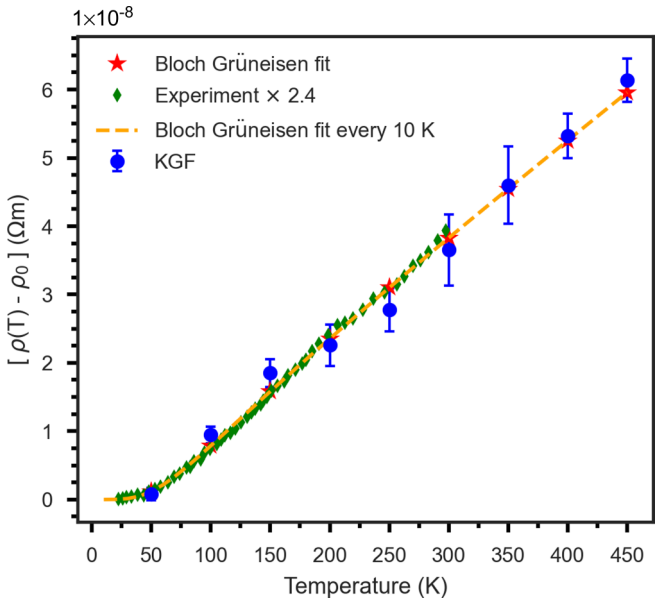

FIG. 2. Resistivity derived from the KGF (smearing width of 0.02 eV) calculated at different temperatures (blue solid circles) and the fitted values using Eq. (6) (red solid stars). The blue bars correspond to standard deviation from the mean resistivity that is computed from the KGF. The orange dashed line is added as a guide for visualization that passes along the fitted values. The experimental data are shown by green solid diamonds taken from Ref. [42]. There is a factor of 2.4 between the calculated and experimental values.

The Bloch-Grüneisen formula is expressed as

$$\rho(T) = \rho_0 + A\left(\frac{T}{\Theta_D}\right)^5 \int_0^{\Theta_D/T} \frac{x^5}{(e^x - 1)(1 - e^{-x})} dx, \quad (6)$$

where ρ_0 is the residual resistivity and is independent of temperature, A is the prefactor of the Bloch-Grüneisen formula and is proportional to the electron-phonon coupling constant, and Θ_D is the Debye temperature of the metal.

The resistivity using the KGF and the fit using the Bloch-Grüneisen formula at selected temperatures are shown in Fig. 2. The calculated and fitted values of resistivity are represented by solid blue circles and solid red stars, respectively. The orange dashed line represents the fit using the Bloch-Grüneisen formula for every 10 K apart to aid visualization. The scattered green solid diamonds correspond to the experimental data. From Fig. 2, we see that the calculated values differ by a factor of ≈2.4 from experiment. We can see that the resistivity provides a good fit to Eq. (6) and is proportional to the T^5 law. For larger supercells that have a relatively narrower splitting of electronic states near E_F, we have the flexibility of using a smaller broadening width that provides better agreement with the experiment. For the current models, we find that the smearing width of 0.005 eV closely agrees with the experiment. For $T < 50$ K, the method fails as the quantum nature of the phonon dominates.

As an illustration to simulate the effect of thermal disorder on conduction, we computed the SPC from two different models, one at 300 K (room temperature) and the other at 900 K (near the melting point). Figure 3 displays SPC as an isosurface color map of an inverted rainbow spectrum obtained from

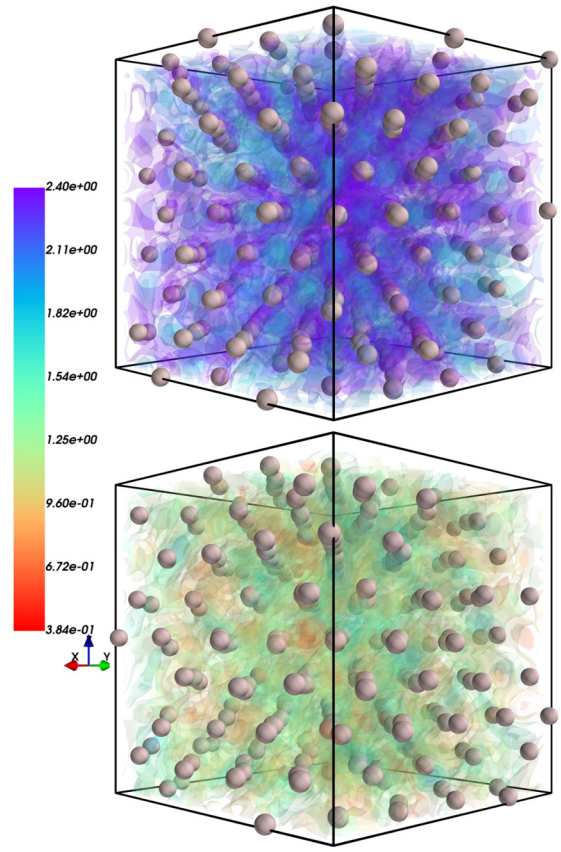

FIG. 3. SPC ζ projected on grids as a color-map plot (units of S/cm) corresponding to different temperatures: room temperature (300 K; top) and near the melting point (900 K; bottom). The inverted rainbow color bar shows the magnitude of SPC scaled with the maximum value at 900 K. The gray spheres represent Al atoms.

those models. The top and bottom plots correspond to 300 and 900 K, respectively. From Fig. 3, it is apparent that a higher reduction of conduction exists at 900 K compared with 300 K. At room temperature, the conduction still appears to be uniform (deep blue and violet in the top plot in Fig. 3), whereas near the boiling point, the conduction is quite random. We see more conduction deficit regions (shown by orange/yellow regions in the bottom plot in Fig. 3) than at room temperature.

B. Spatial distribution of conduction in Al with vacancies

In this section, we discuss the spatial distribution of conduction in aluminum (∼500 atoms model) with single vacancies and divacancies. For this, we computed space-projected conductivity from both types of vacancies as discussed in Sec. II D and visualized it along a few crystallographic planes. We also discuss the directional dependence of the conductivity along those chosen crystallographic planes.

1. Single vacancy

a. 010 plane. Figure 4(a) is a grayscale plot of conductivity projected on the grids closest to the 010 plane of the supercell containing the vacancy. From Fig. 4(a), it is apparent that the primary effect is very local, and the effect decays on moving away from the vacancy. The distance over which the vacancy

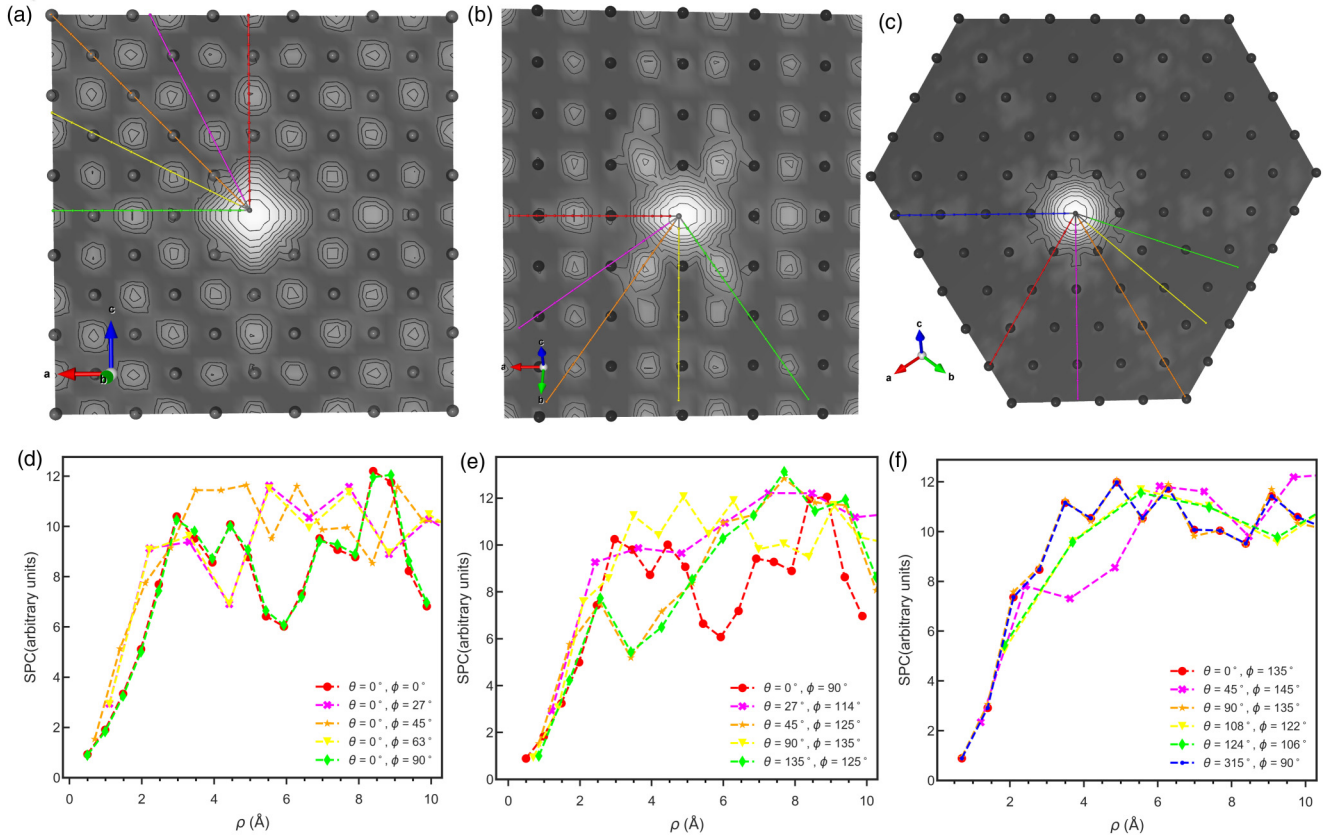

FIG. 4. (a)–(c) Conductivity projected on grids closest to the 010, 011, and 111 crystallographic planes containing vacancy as a 2D grayscale plot. The magnitude of conductivity increases from white to black. The colored lines with small spheres are just for a guide to the eye, representing different directions from the vacancy. (d)–(f) Variation of conductivity with distance from the grid closest to the vacancy along different directions on the 010, 011, and 111 planes, respectively. θ and ϕ refer to the polar and azimuthal angles, respectively. Colors in the legends in (d)–(f) match the lines shown in (a)–(c), respectively.

produces a significant effect on the conductivity can be termed the "reduction range." This distance may also be viewed as the "recovery length" over which the conduction is likely to be recovered after being affected by the defect. For consistency, we pick the latter in the rest of the paper. Figure 4(d) displays the behavior of SPC away from the vacancy at different angles on the 010 plane ($\theta = 0°$). It can be seen that there is slight anisotropy around the vacancy. The recovery length along the axes ($\phi = 0°, 90°$) is ≈2.96 Å. Similarly, along other angles with $\phi = 45°$ and complementary angles ($\phi = 26.56°, 63.44°$), the conduction recovers distances of ≈2.80 and 2.76 Å, respectively. The recovery length along the studied directions is close to first-nearest-neighbor distance (≈2.86 Å), and therefore, the effect of the vacancy can be considered local, as visually observed in Fig. 4(a).

b. 011 plane. Figure 4(b) displays the SPC projected on the 011 plane as a grayscale two-dimensional (2D) plot. On this plane, the effect of vacancy on the conduction spans from the local to intermediate range and has more anisotropy than the 010 plane. Figure 4(e) shows the variation of SPC with distance along different directions on this plane. The conduction along the direction shown by yellow lines in Figs. 4(b) and 4(e) with $(\theta, \phi) = (90°, 135°)$ recovers at a distance of ≈4.1 Å. The recovery length along the direction shown by green lines in Figs. 4(b) and 4(e) with $(\theta, \phi) = (135°, 125°)$ is the longest and is ≈6.0 Å. We see a similar recovery length along $(\theta, \phi) = (45°, 125°)$, which is shown by orange lines in Figs. 4(b) and 4(e).

c. 111 plane. Figure 4(c) is a grayscale plot of SPC projected onto the 111 plane. The effect of the vacancy on this plane also ranges from the local to intermediate range, as observed in the 011 plane. Figure 4(f) shows the variation of SPC with distance along different directions. The recovery length on this plane also varies with direction. The recovery lengths along the directions pointing towards the left and bottom left [blue and red lines in Fig. 4(c)] with $(\theta, \phi) = (315°, 90°)$ and $(0°, 135°)$ are short and are ≈3.5 Å. The recovery lengths along the directions shown by the magenta and green lines with $(\theta, \phi) = (45°, 145°)$ and $(124°, 106°)$ are ≈6.0 Å.

2. Divacancies

a. 010 plane. Figure 5(a) illustrates the SPC projected on the grids closest to the 010 plane with two adjacent vacancies. The spatial distribution of conduction around each vacancy towards the opposite end of either vacancy is similar to the distribution around a single vacancy [see Fig. 4(a)]. The distribution of conduction is dumbbell shaped. Figure 5(d) shows the distribution of SPC from the grid closest to the center of the two adjacent vacancies along different directions. From Fig. 5(d), we see that the distribution is highly anisotropic in nature. Along the z-axis $(\theta, \phi) = (0°, 0°)$, the recovery length

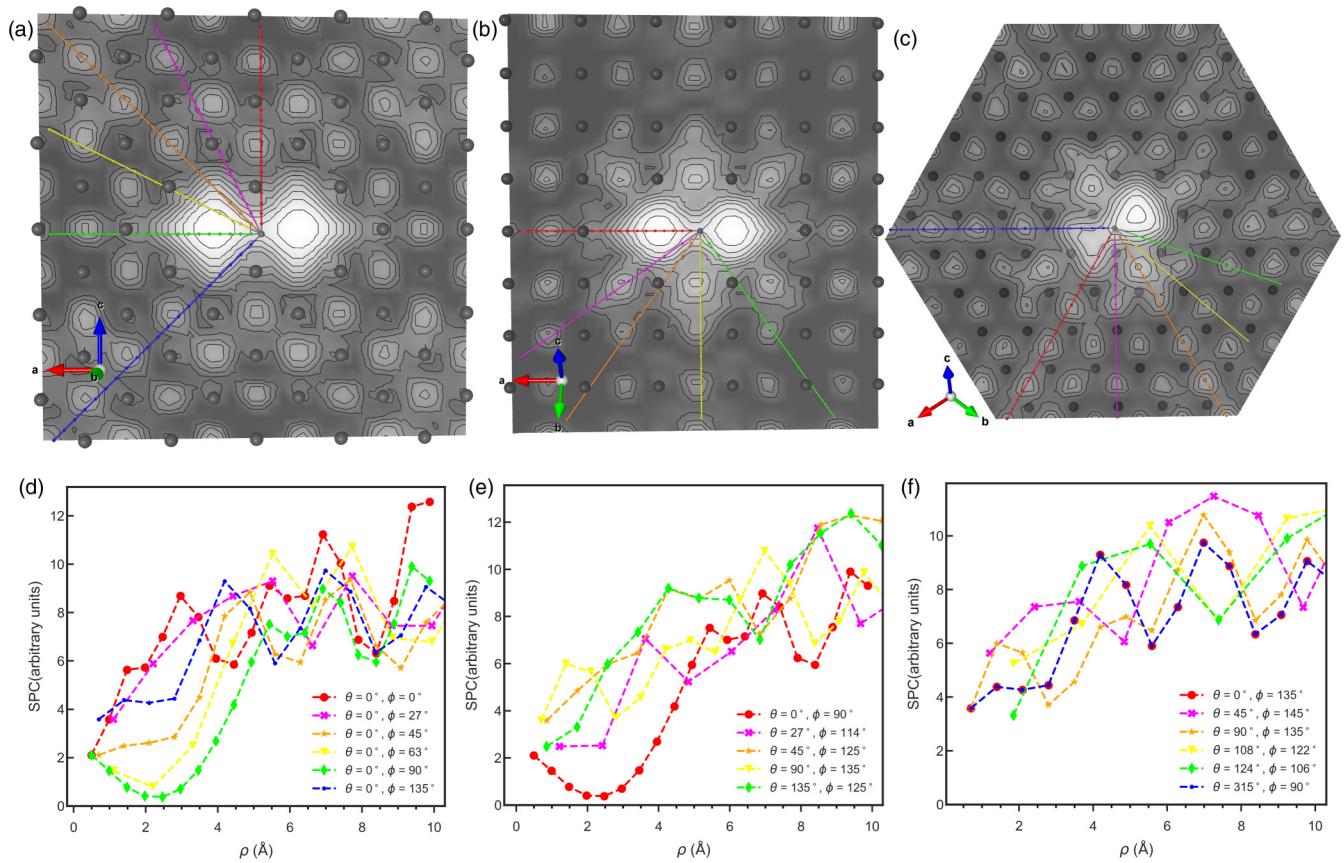

FIG. 5. (a)–(c) Conductivity projected on grids closest to the 010, 011, and 111 crystallographic planes containing the divacancies as a 2D grayscale plot. The magnitude of SPC increases from white to black. The lines with small spheres are just for a guide to the eye, representing different directions from the vacancy. (d)–(f): Variation of conductivity with distance from the grid closest to the center joining two vacancies along different directions on planes 010, 011 and 111 respectively. Colors of legends in (d)–(f) match with the lines shown in (a)–(c) respectively.

of conduction from the center joining the vacancies is ≈6.9 Å. Along the positive x axis $(\theta, \phi) = (0°, 90°)$, the recovery length from the center is ≈9.3 Å, and from the left vacancy it is ≈6.9 Å. Along the direction with $\phi = 27°$, the recovery length is ≈7.7 Å. Along other directions with $\phi = 45°$ and 135°, the recovery length is ≈7.6 Å. The reduction caused by the divacancy is intermediate, and the recovery length is more than twice that for the single vacancy projected on same plane.

b. 011 plane. Figure 5(b) displays the SPC projected on the grids closest to the 011 plane. We can see that the effect of the vacancies is more than the local range along all directions on the plane. The distribution of the conduction towards the opposite end is similar to that of the 010 plane; however, along the other directions, the distribution is different. Figure 5(e) shows the distribution of SPC from the grid closest to the center of the two adjacent vacancies along different directions on this plane. From Fig. 5(e), it is clear that there exists a high degree of anisotropy similar to what was observed in the 010 plane. We find a variation in the reduction along different directions. The recovery lengths are from ≈7.0 to ≈9.3 Å. In other words, the effect of the vacancy is mostly either intermediate or long range in nature. Along directions with $(\theta, \phi) = (27°, 114°), (45°, 125°)$, the recovery length is ≈8.6 Å. Along the direction pointing downwards [yellow line in Fig. 5(b)] with $(\theta, \phi) = (90°, 135°)$, the length is ≈7.0 Å.

c. 111 plane. Figure 5(c) shows the SPC on the grids that are closest to the 111 plane with two adjacent vacancies. The spatial distribution of conduction is quite different near each vacancy. We can see that the reduction is more pronounced near one of the vacancies. Figure 5(f) shows the distribution of the SPC from the grid closest to the center of the two adjacent vacancies along different directions on this plane. From Fig. 5(f), we see that the distribution is highly anisotropic. The recovery length in the direction pointing towards the left [blue line in Fig. 5(c)] with $(\theta, \phi) = (315°, 90°)$ is ≈7.0 Å. The length pointing downwards with $(\theta, \phi) = (45°, 145°)$ in Fig. 5(c) is ≈6.1 Å. Along the directions shown by the yellow and green lines on the right side in Fig. 5(e), the recovery length is ≈5.6 Å.

From the preceding discussion, it is apparent that the spatial distributions of conduction due to single vacancies and divacancies are quite different and vary with the crystallographic directions. The degree of anisotropy is higher for the divacancy relative to the single vacancy. The recovery length for the single vacancy is up to ≈6.0 Å, and that for the divacancy is ≈8.0 Å. The recovery lengths for these studied vacancies are close to the decay length of the density matrix in Al [43].

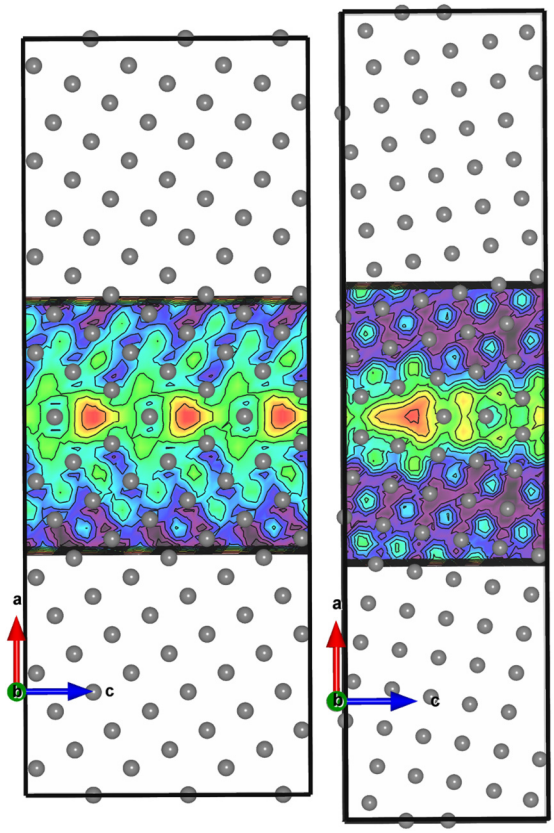

FIG. 6. Two-dimensional plot of SPC projected on a layer of atoms on the 010 plane in the vicinity of the middle grain boundary for two different grain boundary models. Left: Σ5 {0 −3 1} ⟨1 0 0⟩. Right: Σ13 {0 −2 3} ⟨1 0 0⟩. The inverted rainbow colors in both plots represent the magnitude of SPC values, with red corresponding to the small values and violet representing the larger values.

C. Conduction near grain boundaries

In this section, we briefly discuss the spatial distribution of conduction in an aluminum model with GBs. As already described in Sec. II B 2, we chose two symmetric tilt grain boundary models, namely, Σ5 {0 −3 1} ⟨1 0 0⟩ and Σ13 {0 −2 3} ⟨1 0 0⟩. For simplicity, we name these Σ5 and Σ13. For both GB models, we computed the SPC in the vicinity of the middle grain (up to ≈9.0 Å). Figure 6 displays the SPC as a 2D color map projected on the xz plane (i.e., the 010 plane) along a layer of Al atoms for both GB models. The left and right plots correspond to Σ5 and Σ13, respectively. In both plots, the inverted rainbow color maps represent the magnitude of the SPC values, where lower and higher values are shown in red and violet, respectively. It is apparent that the conduction is reduced at the GB, and the effect decays on moving away normally on either side from the GB. For Σ5 (left plot in Fig. 6), the conduction mostly recovers at ≈8.0 Å. On the other hand, the length for Σ13 is close to ≈6.0 Å and is shorter compared with that of Σ5. The recovery length, however, cannot be generalized from these two symmetric boundaries because many types of grain boundaries exist in metals. From Fig. 6, we see that the distribution pattern of the conduction is unique to the particular grain boundary. In both GBs, most reduction occurs in the empty regions that lie at the grain boundaries. One way to improve conductivity in real metals is by reducing the scattering sites that are abundant at the grain boundaries. Experiments have been done interfacing graphene with metals like Al/Cu, and these composites have shown a promising enhancement of the conductivity [44,45].

IV. CONCLUSIONS

In this paper, we utilized the Kubo-Greenwood formula to simulate the temperature dependence of conductivity in aluminum and obtained results in qualitative agreement with the Bloch-Grüneisen formula. We showed that the KGF captures the T dependence down to 50 K. We briefly reviewed a method to project conductivity onto a real-space grid and applied it to study the spatial distribution of conduction in aluminum with thermal disorder and lattice defects. We investigated the effect of conduction in the proximity of single vacancies and divacancies that form prototypes for point defects in the crystal. We computed the range and anisotropy of the conduction reduction. The reduction due to divacancies was shown to involve a longer length scale. We also presented two examples of grain boundaries that are symmetrically tilted. We found that the conduction in such models is reduced at the GB, and the effect decays in a complex way with distance from the GB.

ACKNOWLEDGMENTS

The authors thank Hydro-Innovation and Technology Americas for supporting this work under Research Agreement No. 21043 35528. The authors also acknowledge the Extreme Science and Engineering Discovery Environment (XSEDE), supported by NSF Grant No. ACI-1548562 at the Pittsburgh Supercomputing Center, for providing computational resources under allocation DMR-190008P. Pacific Northwest National Laboratory is operated by the Battelle Memorial Institute for the U.S. Department of Energy under Contract No. DE-AC06-76LO1830. The authors thank Dr. R. Cappelletti for helpful discussions.

[1] L. Boltzmann, in *The Kinetic Theory of Gases* (1872) (World Scientific, Singapore, 2003), pp. 262–349.
[2] E. Lifshitz and L. P. Pitaevskii, *Course of Theoretical Physics* (Butterworth-Heinemann, Oxford, UK, 1981), Vol. 10.
[3] A. Sommerfeld, Naturwissenschaften **15**, 825 (1927).
[4] W. V. Houston, Z. Phys. **48**, 449 (1928).
[5] J. Frenkel and N. Mirolubow, Z. Phys. **49**, 885 (1928).
[6] F. Bloch, Zeitschrift für Physik **52**, 555 (1929).
[7] J. M. Ziman and M. H. L. Pryce, Proc. R. Soc. London, Ser. A **226**, 436 (1954).
[8] R. Kubo, J. Phys. Soc. Jpn. **12**, 570 (1957).
[9] A. Einstein, Ann. Phys. (Berlin, Ger.) **322**, 549 (1905).

[10] A. L. Fetter and J. D. Walecka, *Quantum Theory of Many-Particle Systems* (McGraw-Hill, New York, 1971).
[11] G. D. Mahan, *Many Particle Physics* (Plenum, New York, 1981).
[12] M. J. Stott and E. Zaremba, Phys. Rev. A **21**, 12 (1980).
[13] W. Yang, Phys. Rev. A **38**, 5512 (1988).
[14] P. B. Allen and J. Q. Broughton, J. Phys. Chem. **91**, 4964 (1987).
[15] T. A. Abtew, M. Zhang, and D. A. Drabold, Phys. Rev. B **76**, 045212 (2007).
[16] S. Lowitzer, D. Ködderitzsch, H. Ebert, and J. B. Staunton, Phys. Rev. B **79**, 115109 (2009).
[17] V. Vlček, N. de Koker, and G. Steinle-Neumann, Phys. Rev. B **85**, 184201 (2012).
[18] D. Knyazev and P. Levashov, Comput. Mater. Sci. **79**, 817 (2013).
[19] L. Calderín, V. Karasiev, and S. Trickey, Comput. Phys. Commun. **221**, 118 (2017).
[20] F. Bloch, Zeitschrift für Physik **59**, 208 (1930).
[21] Y. Mishin, M. J. Mehl, D. A. Papaconstantopoulos, A. F. Voter, and J. D. Kress, Phys. Rev. B **63**, 224106 (2001).
[22] R. C. Munoz and C. Arenas, Appl. Phys. Rev. **4**, 011102 (2017).
[23] K. Prasai, K. N. Subedi, K. Ferris, P. Biswas, and D. A. Drabold, Phys. Status Solidi RRL **12**, 1800238 (2018).
[24] K. N. Subedi, K. Prasai, M. N. Kozicki, and D. A. Drabold, Phys. Rev. Mater. **3**, 065605 (2019).
[25] R. Thapa, B. Bhattarai, M. N. Kozicki, K. N. Subedi, and D. A. Drabold, Phys. Rev. Mater. **4**, 064603 (2020).
[26] K. N. Subedi, K. Prasai, and D. A. Drabold, in *The World Scientific Reference of Amorphous Materials* (World Scientific, Singapore, 2021), Chap. 3, pp. 79–105.
[27] K. N. Subedi, K. Prasai, and D. A. Drabold, Phys. Status Solidi B **258**, 2000438 (2021).
[28] S. Nosé, J. Chem. Phys. **81**, 511 (1984).
[29] N. Shuichi, Prog. Theor. Phys. Suppl. **103**, 1 (1991).
[30] D. M. Bylander and L. Kleinman, Phys. Rev. B **46**, 13756 (1992).
[31] V. Randle, *The Role of the Coincidence Site Lattice in Grain Boundary Engineering* (Woodhead, Cambridge, 1997).
[32] M. A. Tschopp, S. P. Coleman, and D. L. Mcdowell, Integr. Mater. Manuf. Innovation **4**, 176 (2015).
[33] Y. Mishin, D. Farkas, M. J. Mehl, and D. A. Papaconstantopoulos, Phys. Rev. B **59**, 3393 (1999).
[34] G. Kresse and J. Hafner, Phys. Rev. B **47**, 558 (1993).
[35] G. Kresse and D. Joubert, Phys. Rev. B **59**, 1758 (1999).
[36] J. P. Perdew, K. Burke, and M. Ernzerhof, Phys. Rev. Lett. **77**, 3865 (1996).
[37] D. A. Greenwood, Proc. Phys. Soc. **71**, 585 (1958).
[38] R. M. Feenstra and M. Widom, https://www.andrew.cmu.edu/user/feenstra/wavetrans.
[39] P. Bulanchuk, Comput. Phys. Commun. **261**, 107714 (2021).
[40] C. M. Van Vliet, *Equilibrium and Non-equilibrium Statistical Mechanics* (World Scientific, Singapore, 2008).
[41] J. M. Ziman, *Electrons and Phonons: The Theory of Transport Phenomena in Solids*, Oxford Classic Texts in the Physical Sciences (Oxford University Press, New York, 1960).
[42] A. Chowdhury and S. Bhattacharjee, J. Phys. D **46**, 435304 (2013).
[43] X. Zhang and D. A. Drabold, Phys. Rev. B **63**, 233109 (2001).
[44] W. Li, D. Li, Q. Fu, and C. Pan, RSC Adv. **5**, 80428 (2015).
[45] M. Cao, Y. Luo, Y. Xie, Z. Tan, G. Fan, Q. Guo, Y. Su, Z. Li, and D.-B. Xiong, Adv. Mater. Interfaces **6**, 1900468 (2019).